

## **Simulating the effects of carbon nanotube continuity and interfacial bonding on composite strength and stiffness**

Benjamin D. Jensen<sup>a\*</sup>, Gregory M. Odegard<sup>b</sup>, Jae-Woo Kim<sup>c</sup>, Godfrey Sauti<sup>a</sup>, Emilie J. Siochi<sup>a</sup>, Kristopher E. Wise<sup>a</sup>

<sup>a</sup> Advanced Materials and Processing Branch, NASA Langley Research Center, Hampton, VA USA

<sup>b</sup> Department of Mechanical Engineering - Engineering Mechanics, Michigan Technological University, Houghton, MI USA

<sup>c</sup> National Institute of Aerospace, Hampton, VA USA

\*Corresponding author: Benjamin Jensen, [benjamin.d.jensen@nasa.gov](mailto:benjamin.d.jensen@nasa.gov)

### **ABSTRACT**

Molecular dynamics simulations of carbon nanotube (CNT) composites, in which the CNTs are continuous across the periodic boundary, overestimate the experimentally measured mechanical properties of CNT composites along the fiber direction. Since the CNTs in these composites are much shorter than the composite dimensions, load must be transferred either directly between CNTs or through the matrix, a mechanism that is absent in simulations of effectively continuous CNTs. In this study, the elastic and fracture properties of high volume fraction discontinuous carbon nanotube/amorphous carbon composite systems were compared to those of otherwise equivalent continuous CNT composites using ReaxFF reactive molecular dynamics simulations. These simulations were used to show how the number of nanotube-matrix interfacial covalent bonds affect composite mechanical

properties. Furthermore, the mechanical impact of interfacial bonding was decomposed to reveal its effect on the properties of the CNTs, the interfacial layer of matrix, and the bulk matrix. For the composites with continuous reinforcement, it was found that any degree of interfacial bonding has a negative impact on axial tensile strength and stiffness. This is due to disruption of the structure of the CNTs and interfacial matrix layer by the interfacial bonds. For the discontinuous composites, the modulus was maximized between 4%-7% interfacial bonding and the strength continues to increase up to the highest levels of interfacial bonding studied. Areas of low stress and voids were observed in the simulated discontinuous composites at the ends of the tubes, from which fracture was observed to initiate. Experimental carbon nanotube yarn composites were fabricated and tested. The results were used to illustrate knockdown factors relative to the mechanical performance of the tubes themselves.

**KEYWORDS:** Carbon nanotubes, ReaxFF, molecular dynamics, fracture, nanocomposite

## 1.0 INTRODUCTION

From improving the efficiency of atmospheric flight to enabling more affordable and capable deep space mission designs, ongoing advances in lightweight, high performance structural materials are critical to progress in aerospace vehicle development. Decades of focused research and development have produced a range of highly optimized conventional carbon fiber composites with mechanical properties that are beginning to plateau. As a result, attention has turned to materials that have the potential to eventually surpass the properties of state of the art carbon fiber composites [1]. Carbon nanotubes (CNTs), for example, have been shown by modeling and nano/micro-scale measurements to have much

higher specific strength and stiffness than carbon fibers [2–4]. In recent years, rapid advances in manufacturing and processing have led to the availability of large quantities of high quality CNTs in practically useful material formats, such as large sheets and kilometer-length yarns [5–7]. As a result, it is now possible to fabricate high volume fraction CNT composites with specific strength and stiffness values that approach those of current aerospace carbon fiber composites [6–9]. These properties are achieved in samples with notably non-optimal microstructures: they exhibit large voids, both within and between the reinforcing yarns [6]. Optimization of the composites will require ongoing improvements in both modeling and experimental methods to address their hierarchical nature: CNTs have important features on length scales ranging from 1 nm (their typical diameter) to 1 mm (their length), to even larger scales (bundles, fibers, and composites) [10–12].

This work used molecular dynamics simulations to predict the mechanical properties of composites composed of CNTs in an amorphous carbon matrix. The newly predicted elastic and fracture behaviors of discontinuous CNT/amorphous carbon composites were compared with continuous CNT analogs reported previously [13]. As in the previous work, amorphous carbon was selected as the matrix material to both reduce the complexity of constructing and equilibrating the model structure, relative to the use of a polymer matrix, and because it permitted the use of a well-validated reactive force field in the molecular dynamics simulations. Additionally, amorphous carbon is relevant to the experimental material as it is often found in CNT sheets and yarns as a byproduct of the synthesis process [14]. Since amorphous carbon is stiffer and stronger than polymer matrices, these

results represent an upper bound on several properties typical of CNT-polymer matrix composites.

While the length of the discontinuous tubes used in these simulations, 22.1 nm, is much smaller than in the experimental material, they are quite long compared to those in previous simulation work. Our new studies have also added CNT-matrix linking, and used a method capable of modeling material failure [15,16]. Simulations of direct linking between CNTs improved the mechanical properties relative to systems without bonds [17–23]. Other work using the ReaxFF reactive force field, which is capable of modeling covalent bond breaking [24,25], has examined the mechanical properties of allotropic carbon systems [26,27] and continuous CNT/amorphous carbon composites [13]. The present paper goes beyond this previous work by simulating the mechanical deformation to failure of reasonably long but discontinuous CNTs chemically linked to an amorphous carbon matrix.

## 2.0 COMPUTATIONAL DETAILS

The molecular dynamics simulations were performed using the reactive force field ReaxFF [24,28], as implemented in the LAMMPS molecular dynamics package [29,30]. The ReaxFF<sub>C-2013</sub> parameters, originally developed to investigate fullerene formation, were used in this work [25]. The ReaxFF<sub>C-2013</sub> parameters have previously been used to study single- and multi-walled nanotube composites [13], nanoparticle impacts on graphene [31], CNT vacancies [32], and they have been incorporated into expanded parameter sets [33–36]. The reliability of the ReaxFF<sub>C-2013</sub> parameterization for predicting the elastic and fracture properties of diamond, graphene, amorphous carbon, and carbon nanotubes has been validated previously by comparison with experimental measurements and density

functional theory results [26]. Molecular structure images were rendered using the Ovito visualization software package [37].

Molecular models of the continuous and discontinuous CNT/amorphous carbon matrix composites are shown in Fig. 1. Here, Fig. 1a depicts the continuous system in which the CNTs continue through the periodic boundaries of the 10.2 nm long simulation cell. The discontinuous system, shown in Fig. 1b, is composed of 22.1 nm long CNTs terminated with hemispherical end-caps. A longer box length was used in the discontinuous systems to increase the CNT aspect ratio. The discontinuous CNTs were offset to maximize the distance between adjacent CNT ends. The axial length of the simulation cell was 24.0 nm resulting in ~2 nm of matrix between the endcaps of each CNT. All systems had a CNT mass fraction of 37%. All CNTs had a chirality of (20,0) and a diameter of ~1.56 nm. The atoms in each system were grouped into four constituent groups for analysis purposes, as indicated by coloring in Fig. 1.

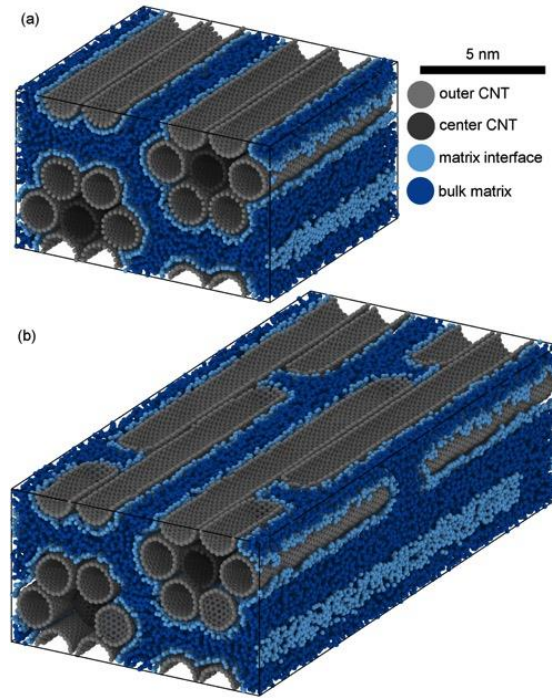


Fig. 1. Equilibrated systems composed of (a) continuous CNTs and (b) discontinuous CNTs. Atoms are colored according to their structure.

For both continuous and discontinuous systems, five models were created with CNT-matrix interfacial bonding fractions of approximately <1%, 5%, 10%, 15%, and 20%. These correspond to number densities of approximately 0.0, 1.9, 3.8, 5.7, and 7.6 bonds/nm<sup>2</sup>, respectively. Additional description of the systems is provided in the supplemental information. To assess the dependence of the predicted properties on initial configurations, two independent systems were created at each interfacial bonding fraction, resulting in a total of 20 independent simulated systems. Each system was created using an equilibration procedure that lasted for 607 ps, as described in [13].

All mechanical properties in this work are reported in specific units of GPa/(g/cm<sup>3</sup>), which is volume independent and can be reduced to N/(g/km) or N/tex, which is the unit commonly used in the fiber community. Specific stiffness tensors ( $\mathbf{C}$ ) were computed from

$$\bar{\sigma}_c = \mathbf{C} \varepsilon_g \quad (1)$$

where  $\bar{\sigma}_c$  is the average specific stress in the constituent and  $\varepsilon_g$  is the global strain.

Engineering constants are then computed from the stiffness tensor in the standard manner [38]. This tensor, referred to as the *effective intermediate modulus tensor* in the literature, is a good approximation of the local stiffness when the strains in the system are homogenous [39,40]. For the continuous CNT models, the strains of the bulk matrix, matrix interface, and continuous CNTs are directly coupled to the global strains, being continuously connected across the periodic boundaries. It is reasonable to expect that the strains in these constituents can be approximated as the global strains. This is not the case for the discontinuous CNTs, as the deformation of the CNTs fails to track the overall deformation of the composite due to the formation of voids at the tube ends. The treatment of this void space in the calculation of the constituent moduli in the discontinuous systems is somewhat ambiguous, and various approaches have appeared in the literature (see supplementary information). The results presented in this paper used the actual change in discontinuous CNT length during the tensile simulation in calculating the CNT constituent axial strain. The elastic modulus was taken to be the slope of the best fit line, up to 1% strain, of a plot of CNT specific stress against CNT strain, using this strain definition.

### 3.0 RESULTS

#### 3.1 INTERFACE STRUCTURING

As mentioned in Section 2, the matrix atoms were subdivided into an interfacial group and a bulk matrix group. Removal of portions of the CNTs from the visualization, as shown in Fig. 2a and Fig. 2b, reveals the structuring that was induced in the interfacial region by the CNTs during the heating and equilibration phases of the structure building process. This interfacial surface was composed of a mixture of connected fused ring systems of varying sizes and resembles a highly defective CNT.

Cylindrical distribution functions were computed, as described in the supplemental information, to permit a quantitative description of interfacial structuring. Fig. 2c compares the structure of the matrix at the lowest extent of interfacial bonding for continuous and discontinuous systems. Both systems were found to have large peaks at  $\sim 0.34$  nm, corresponding to the first structured interface layer, followed by a second, smaller peak at approximately 0.68 nm. Beyond the second peak, the cylindrical distribution function plateaued to the bulk matrix value. The less pronounced peaks found in the discontinuous system reflect the less structured interface seen in Fig. 2b. Here, Fig. 2d shows the cylindrical distribution function for the continuous systems at different interfacial bonding fractions. The magnitude of the peak was greatest in the  $<1\%$  system, and steadily decreased until essentially all interfacial structure is lost at 18% interfacial bonding. The peak was also observed to shift to shorter distances as interfacial bonding increased. The impact of this ordered interfacial layer on composite mechanical properties is discussed in more detail below.



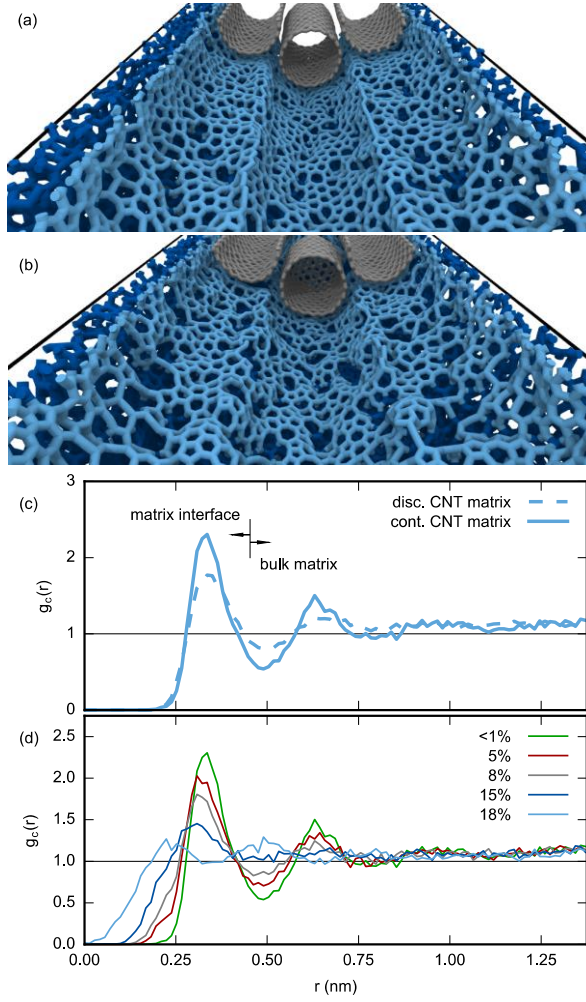


Fig. 2. Matrix interface surface of the <1% bonded (a) continuous and (b) discontinuous systems. A portion of the CNT atoms have been hidden to expose the interfacial matrix layer. (c) cylindrical distribution functions comparing <1% bonded discontinuous and continuous systems, and (d) continuous systems with different amounts of interfacial bonding. Atoms in (a) and (b) are colored according to their structure as in Fig. 1.

### 3.2 ELASTIC PROPERTIES

The dependence of the axial elastic moduli of the continuous and discontinuous CNT composites on the degree of interfacial bonding is shown in Fig. 3a. The modulus of the

continuous system was highest in the model with <1% bonding, and steadily decreased as the degree of bonding increased. While the interfacial bonds effectively acted as defects in the CNTs, there exists an optimal degree of bonding in the discontinuous composites that maximizes load transfer while minimizing damage to the CNTs, and disruption of the structured matrix interface. Rather than being a linearly decreasing function of the degree of interfacial bonding, as was the case for the continuous composite, the moduli of the discontinuous composites were highest between 4% and 7% bonding, where the moduli were 131 and 133 GPa/(g/cm<sup>3</sup>).

The specific axial moduli of the central and outer CNT constituents are compared in Fig. 3b. The stiffness of the continuous outer CNTs, to which all interfacial bonds were formed, fall by 28% for increasing degrees of bonding. The continuous central CNTs, which were shielded from interfacial bonding, were unaffected by matrix bonding to the outer CNTs. At <1% interfacial bonding, the discontinuous outer CNTs were not sufficiently bonded to the matrix to be strained during the tensile deformation, which prevents reliable calculation of a modulus. With 4% or more interfacial bonding, the discontinuous outer CNTs become sufficiently mechanically connected to the composite to achieve measurable strains. These discontinuous CNTs behaved similarly to the continuous outer CNTs: their moduli decreased due to disruption of the CNT structure by the interfacial bonds. The central CNTs of the discontinuous system are not shown in Fig. 3b because they were unconnected to the matrix, and were not strained by the overall deformation of the composite.

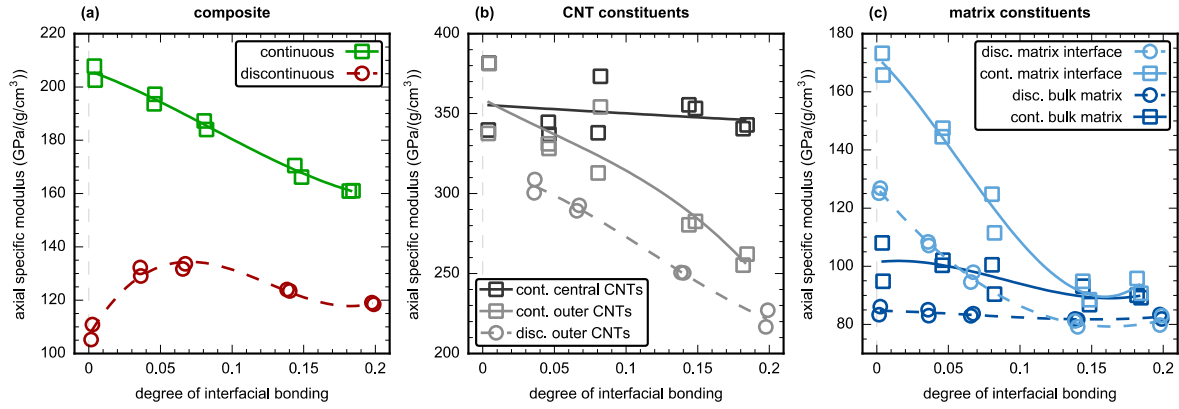


Fig. 3. Axial moduli of (a) composites, (b) CNT constituents, and (c) matrix constituents as a function of degree of interfacial bonding. The colors of the constituents in (b) and (c) match the structures in Fig. 1. Trendlines are a guide to the eye.

The trends in the moduli of the interfacial matrix constituents, shown in Fig. 3c, followed trends very similar to those of the outer CNTs. For both the continuous and discontinuous systems, the highest moduli were found for the least bonded systems, and they decreased when interfacial bonds were introduced. This was because of the trend in structural ordering that is quantified with the cylindrical distribution function in Fig. 2d. At the highest degrees of interfacial bonding, both the structural ordering and the elastic moduli approached the values for the bulk matrix. The magnitude of the moduli for the discontinuous systems were lower at each degree of interfacial bonding, which was a reflection of the lower average degree of order shown in Fig. 2c. For both the continuous and discontinuous systems the moduli of the bulk matrices were essentially the same regardless of the extent of interfacial bonding. This is not surprising as the bulk matrix was defined previously from the density distribution function to exclude the structured interface.

These results indicate that the elastic modulus can be maximized by keeping interfacial bonding to a minimum for composites reinforced with very high aspect ratio CNTs.

Composites reinforced with shorter tubes, however, will benefit from a moderate degree of interfacial bonding. The remaining elastic constants, shear moduli, and Poisson's ratios, are included in supplemental information.

### 3.3 FRACTURE PROPERTIES

The axial stress-strain responses of the composites and constituents (shown in columns) at different degrees of interfacial bonding (shown in rows) are plotted in Fig. 4, in which maximum stresses are marked with 'X' symbols. As shown in these figures, the maximum stress experienced by a constituent does not always coincide with that of the other constituents in the same system, or the overall composite. For example, in the 18% bonded continuous system (center column of the bottom row), the central CNT, which was not bonded to the matrix, broke at a much higher strain and stress than either the matrix, or the outer CNTs. Because the central CNT is a minor component of the overall composite (~5% by mass), the composite properties, shown in the green line in the first column of the bottom row, were dominated by the ultimate properties of the matrix and outer CNTs.

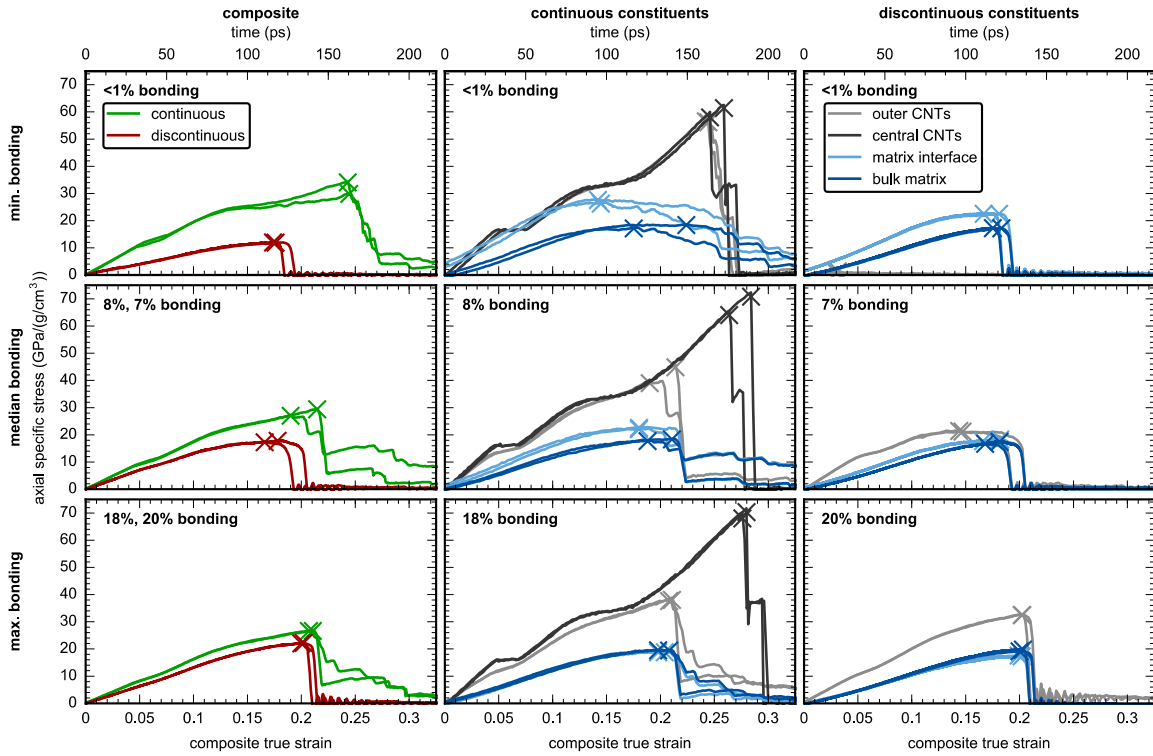


Fig. 4. Axial stress-strain responses of continuous and discontinuous composites and their constituents at a range of interfacial bonding. Maximum stresses are indicated with ‘X’ symbols. The central CNTs in the discontinuous systems are not shown as their stresses are near zero.

For the <1% bonded systems shown in the top row of Fig. 4, the maximum strain of the continuous composite was determined by the CNTs, while the matrix appeared to limit the maximum stress. For the discontinuous composite, the CNTs that were essentially disconnected from the composite, have an overall negative impact on composite properties. This can be seen by comparing the top left and top right panels, which show that the discontinuous composite had a lower strength than its matrix constituents, due to the mass of CNTs that did not contribute to structural reinforcement.

At the intermediate levels of interfacial bonding shown in the middle row of Fig. 4, the strengths of the continuous and discontinuous composites have begun to converge, as shown in the left panel. The middle panel shows that the unbonded central CNTs in the continuous system retained their pristine properties, while interfacial bonding reduced the strength of both the outer CNTs and the matrix interface. In the discontinuous system, shown in the right panel, interfacial bonding led to an increase in the stress in the outer CNTs, a decrease in the matrix interface stress, and had no effect on stress in the central CNT.

Finally, at the maximum level of interfacial bonding shown in the bottom row of Fig. 4, the composite properties of the two systems were nearly equal. This was a result of the continued weakening of the outer CNTs and matrix interface in the continuous system, shown in the middle panel, and the increasing load transfer to the outer CNTs in the discontinuous system, shown in the right plot. Similar plots for axial deformation at the other degrees of interfacial bonding, as well as plots of the results for tensile deformation simulations conducted in the transverse directions, are provided in the supplemental information.

The composite and constituent maximum axial stresses for all interfacial bonding fractions are summarized in Fig. 5. As illustrated in Fig. 5a, increasing the degree of interfacial bonding had very different effects on the continuous and discontinuous systems. While increasing interfacial bonding resulted in a 16% decrease in the strength of the continuous composite, the discontinuous composite strength increased by 85%. Focusing on the contributions of the central and outer CNTs, Fig. 5b shows that the strength of the central

tubes, which were not bonded to the matrix, was unaffected by the interfacial bonding of the outer tubes. The outer tubes, on the other hand, reflect the changes seen in the overall composite properties. Specifically, the strengths of the outer tubes in the continuous composite decreased by 32%, while those in the discontinuous composite increased from essentially 0 to 28 GPa/(g/cm<sup>3</sup>). As in the case of the elastic properties, the interfacial matrix constituents behaved similarly in the two composites, although the more highly structured interface in the continuous system is reflected in its 16% higher strength at <1% interfacial bonding and its slower convergence to bulk properties with increasing interfacial bonding. The strength of the bulk matrix was rather insensitive to the extent of interfacial bonding, having a specific maximum stress approximately 18 GPa/(g/cm<sup>3</sup>) in both the continuous and discontinuous systems.

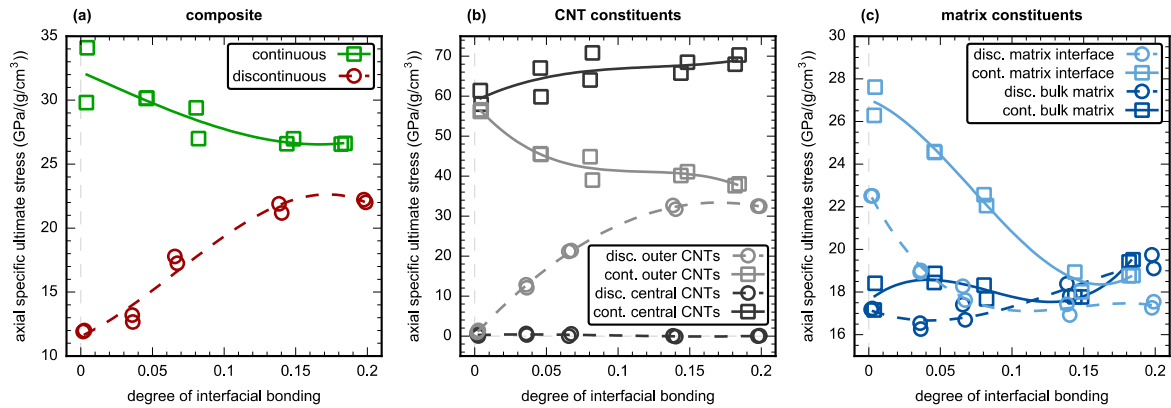


Fig. 5. Comparison of continuous and discontinuous CNT maximum axial specific stresses for the (a) composite, (b) CNT constituents, and (c) matrix constituents. Trendlines are a guide to the eye.

For the continuous composite, the trends in maximum tensile stress were very similar to those found for the specific tensile modulus: the largest values were found for the <1%

interfacial bonding system, and steadily decreased with increasing degree of interfacial linking. The strength of the discontinuous composite continued to increase until it plateaued at around 14% interfacial bonding. The specific modulus reached a peak value at around 5%, followed by a steady decrease with additional interfacial bonding. This indicates that the extent of interfacial bonding may be used to tailor a composite to maximize strength or stiffness, although tight control over the process is required. In experimental composites where the bundle sizes are larger, the mass fraction of central CNTs is higher, and therefore their mechanical response will have a larger influence on the overall composite response.

### 3.4 STRESS DISTRIBUTION IMAGES

The distribution of stresses within the composite structures are shown in Figs. 6 and 7, with atoms colored according to the axial component of their specific stress tensors. Since the results in this paper are given in specific units, the stresses shown are properties of the atoms, and do not require the specification of physically ambiguous atomic volumes, as is the case when using non-specific stress. Diversity of local atomic bonding configurations and thermodynamic fluctuations produced substantial variability in the atomic specific stress values. To improve interpretability, the values depicted in Figs. 6 and 7 were averaged over several consecutive time steps, and over neighboring atoms within 0.19 nm.

The stress distributions for the composites with the minimum, median, and maximum interfacial bonding are shown at 18% strain in Fig. 6. The highest stresses in the continuous CNT composites were found in the <1% bonded continuous system, and show a decreasing trend with the extent of interfacial bonding. The distribution of stresses along the continuous CNTs was reasonably homogenous, as expected for a random distribution of



interfacial bond sites, although some larger stress concentrations were found in the most bonded system, due to the agglomeration of neighboring bonds that act as a larger defect. In the discontinuous systems, the <1% bonded CNTs exhibited essentially no stress buildup, which was consistent with the negligible stress noted for this system in Fig. 4 and Fig. 5. The stress began to build in the outer CNTs at an interfacial bonding fraction of 7%, eventually resembling that of the continuous systems, for the 20% bonded composite. In contrast to the continuous system, the stress distribution along the length of the CNTs varied, with the center of the CNTs having a much higher stress than the ends. This is due to the load transfer through the individual interfacial bonds, with each bond resulting in an increase in axial CNT stress from the ends of the CNT towards the center. A similar stress distribution is predicted by micromechanics models of discontinuous fibers wherein load is transferred to the fibers through a continuous interface [38]. This effect was particularly pronounced in the 7% bonded system, although it was also observed near the ends of the CNTs in the 20% bonded system. As was found in the continuous composites, the most bonded discontinuous CNTs had clear local stress concentrations.

In both the continuous and discontinuous systems, the stresses in the matrix were much less uniform than in the CNTs. This was likely due to the existence of a wide variety of bonding geometries in the amorphous matrix, as opposed to the more highly oriented, crystalline bonds of the CNTs. The matrix stresses were relatively homogenous in the continuous composites. In the discontinuous systems, it was clear that the stresses in the matrix between CNT endcaps were lower, and the regions between adjacent bundles were similar in appearance to the continuous composites.

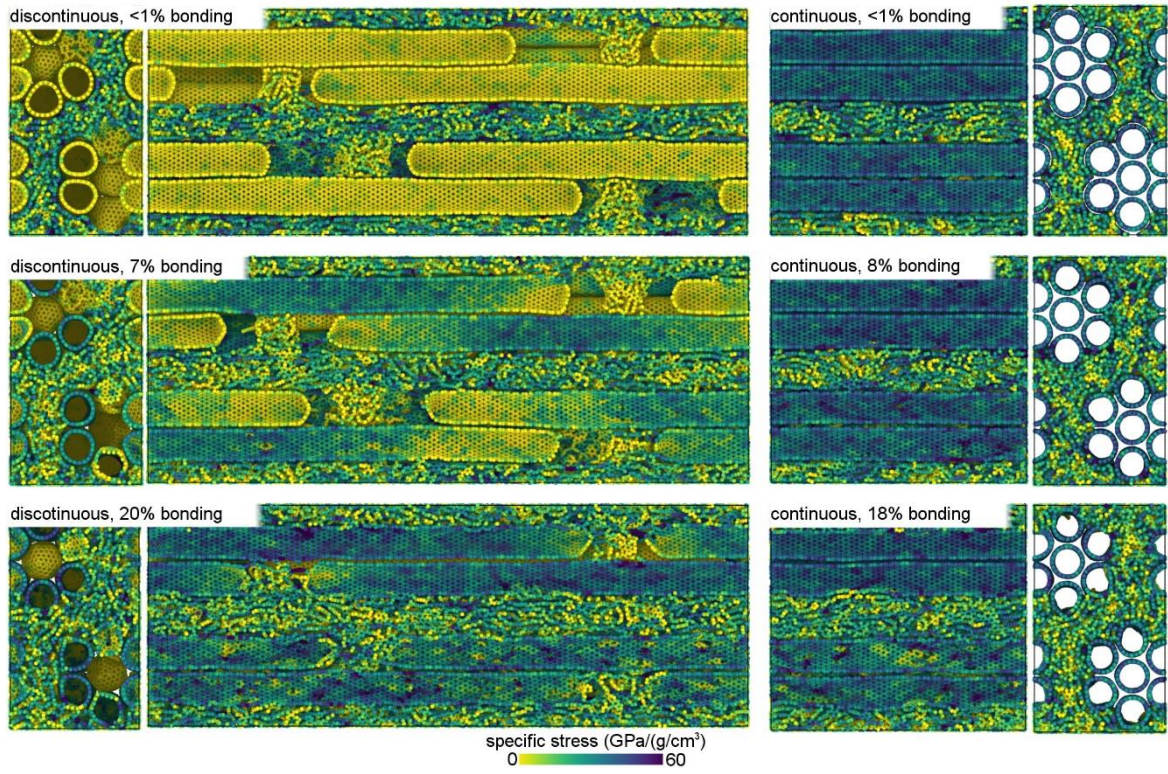


Fig. 6. Stress distributions in continuous and discontinuous systems at 18% strain.

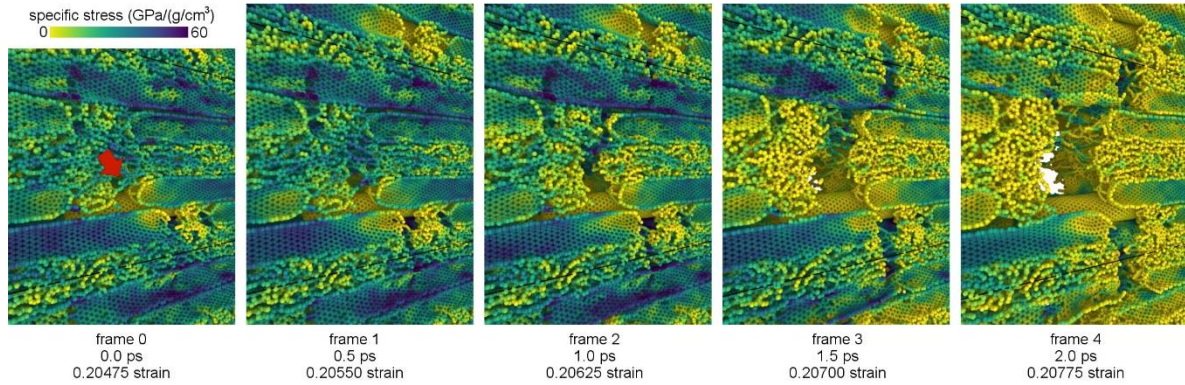


Fig. 7. Void formation and fracture initiation in a 20% bonded discontinuous system.

Five snapshots from the simulation at times immediately preceding the initiation of fracture in the 20% bonded discontinuous system are shown in Fig. 7. The first frame shows that the lowest atomic specific stresses in the pre-fracture state were found at the CNT ends, which

separated from the matrix slightly. This small void between the endcap and matrix, marked with a red arrow in left-most panel of Fig. 7, served as a fracture nucleation point. As the composite strain increases, a void grew from the lower bundle towards the upper bundle, eventually bridging completely between the two endcap voids as the system severs completely. This endcap void nucleation mechanism contributes to the lower fracture strength of the discontinuous systems, although to a lesser degree than the CNT-matrix interfacial strength, which dominates the fracture strength of the composites.

### 3.5 COMPARISON WITH EXPERIMENT

To facilitate comparison of the simulated systems with experimental materials, a carbon nanotube yarn composite was fabricated and tested. The CNT yarn composite was fabricated by infiltrating a nanotube yarn (Nanocomp Technologies, Inc.) with a bismaleimide (BMI) polymer matrix (RM-3010, Renegade Materials Corp.) to yield a composite that is 18 wt.% polymer. Additional composite fabrication and mechanical testing data are published elsewhere [41,42], and in the supplemental information.

The axial specific moduli and maximum specific stresses of the discontinuous and continuous composites, and of the CNT constituents reported in the previous sections are plotted together in Fig. 8a. Each symbol represents an average of the five interfacial bonding fractions. Experimental values for an individual multiwall carbon nanotube (MWCNT) [2], a single wall carbon nanotube (SWNT) bundle [3], a short CNT yarn [43], and the CNT yarn composite from this work are shown in Fig. 8b. The CNT yarn composite had a specific strength and stiffness of  $1.461 \pm 0.185$  and  $75.4 \pm 10.1$  GPa/(g/cm<sup>3</sup>), respectively, which are 97% and 84% lower than the experimentally measured properties

(45 and 468 GPa/(g/cm<sup>3</sup>)) for single MWCNT strength and stiffness, respectively. Note that the individual MWCNT values are plotted in specific units in Fig. 8, but correspond closely to the commonly cited maximum non-specific strength and stiffness values of 100 GPa and 1 TPa, respectively. Details of the conversion to specific values are provided in the supplemental information.

The data plotted in Fig. 8b shows the property knockdowns that are commonly encountered when scaling materials from nano-scale testing to larger and more complex material forms. These experimental samples are helpful in evaluating the relative importance of the simulated mechanical property knockdown mechanisms, and illustrate the challenges involved in translating individual CNT properties to a macroscale CNT yarn composite. The experimental knockdown from the individual CNT to the CNT bundle was a 75% reduction in specific strength, but only a 4% reduction in specific modulus. The simulations showed a similar trend for the knockdown on going from pristine to bonded CNTs, with reductions of 32% in specific strength and 11% in specific modulus. The greater strength knockdown in the experimental results may indicate a larger extent of damage to these CNTs than what was caused by the interfacial bonding in the simulations. Overall simulated continuous composite strength and modulus are 35% and 41% lower than the corresponding properties of just the bonded CNT constituents. Finally, the lowest simulated properties were for the discontinuous composite, which was 61% lower in both specific strength and stiffness than the bonded CNTs, and 74% and 65% lower than the pristine CNT values, respectively.



Practical limitations on the volume of material that can be simulated at the atomistic level prevent the inclusion of microscale features such as entanglements, voids, and large-scale bundles that were observed in the experimental material [44,45]. As a result, the present simulations cannot address their relative contributions to the substantial reductions in specific strength and modulus that are found in the experimental materials, going from the CNT bundle to the short yarn and yarn composite samples. There were many additional differences between the simulated material and the experimental yarn composite, including matrix material, CNT volume fraction, CNT length and diameter, CNT misalignment, strain rate, and system size. The experimental yarns also contain impurities such as iron catalyst particles, graphitic cages, oxygen, and various functional groups not present in the simulation [14]. As a result, quantitative agreement cannot yet be expected when making comparisons of the simulated and experimental composites.

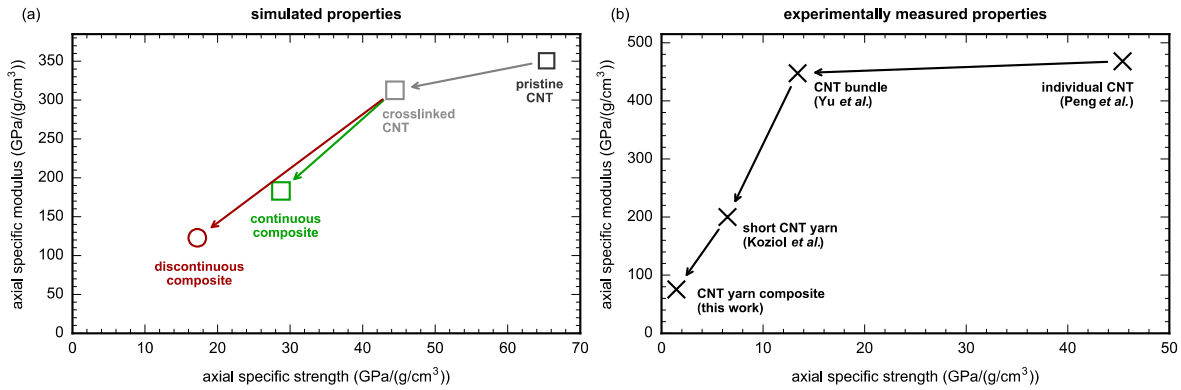


Fig. 8. (a) Trends of the averaged simulated composite and constituent CNT specific strength and modulus. (b) Trends of specific strength and modulus of experimental CNTs at various length scales. Individual MWCNT properties are from ref. [2], SWCNT bundle from ref [3], short CNT yarn from ref [43], and CNT yarn composite from this work.

## 4.0 CONCLUSIONS

Molecular dynamics simulations were performed on high volume fraction, continuous and discontinuous CNT/amorphous carbon composite systems with CNT-matrix covalent linking fractions ranging from 0-20% of the outer tube atoms. This work led to several interesting insights.

First, a mechanically significant structuring of the amorphous carbon matrix at the CNT interface was observed and characterized. This layer was found to have 48-68% higher axial specific stiffness and 35-50% higher maximum stress than the bulk matrix in the <1% bonded systems. At higher degrees of interfacial bonding, the mechanical properties of the interface layer decreased, until they become equal to those of the bulk matrix at 15% interfacial bonding.

Second, the highest composite axial elastic modulus in the continuous CNT systems was found in the <1% bonded system and it was steadily decreased by increasing interfacial bonding. The maximum modulus for the discontinuous systems was found for an intermediate degree of interfacial bonding of 4%-7%.

Third, the maximum axial tensile stress found for the continuous CNT composites occurred in the <1% bonded system, and stresses were lowest in the 18% bonded system. The discontinuous composites were found to have their lowest strength at <1% interfacial bonding and their strengths increased continuously with interfacial bonding, reaching a maximum quite close to that of the similarly bonded continuous system.

Finally, areas of low stress were observed at the ends of the discontinuous tubes, and in the matrix between them. Interfacial bonding decreased the extent of these areas and localized them at the ends of the tubes. Under loading, voids invariably formed in these low stress regions, creating initiation sites for material failure.

While morphological and other differences in the present simulations prevent quantitative comparison with experimental fibers, qualitative comparisons offer some insight into the relative importance of the various simulated property reduction mechanisms. Comparing the nano-scale experimental knockdown from individual CNTs to a bundle, to the simulated CNT interfacial bonding knockdown, both decreased in strength much more than modulus. The experimental knockdown in strength was also much larger than the simulated crosslinking knockdown indicating that the damage was more severe in the experimental sample. The remaining experimental knockdown to macroscale composites gives an indication of the importance of features beyond the nanoscale such as entanglements and voids.

## REFERENCES

- [1] E.J. Siochi, J.S. Harrison, Structural nanocomposites for aerospace applications, *MRS Bull.* 40 (2015) 829–835. doi:10.1557/mrs.2015.228.
- [2] B. Peng, M. Locascio, P. Zapol, S. Li, S.L. Mielke, G.C. Schatz, H.D. Espinosa, Measurements of near-ultimate strength for multiwalled carbon nanotubes and irradiation-induced crosslinking improvements, *Nat. Nanotechnol.* 3 (2008) 626–631. doi:10.1038/nnano.2008.211.
- [3] M.-F. Yu, B.S. Files, S. Arepalli, R.S. Ruoff, Tensile Loading of Ropes of Single Wall Carbon Nanotubes and their Mechanical Properties, *Phys. Rev. Lett.* 84 (2000) 5552. doi:10.1103/PhysRevLett.84.5552.
- [4] B.G. Demczyk, Y.M. Wang, J. Cumings, M. Hetman, W. Han, A. Zettl, R.O. Ritchie, Direct mechanical measurements of the tensile strength and elastic modulus of multi-walled carbon nanotubes., *Mater. Sci. Eng. A.* 334 (2002) 173–178. doi:http://dx.doi.org/10.1016/S0921-5093(01)01807-X.
- [5] M.F.L. De Volder, S.H. Tawfick, R.H. Baughman, A.J. Hart, Carbon nanotubes:

- present and future commercial applications, *Science*. 339 (2013) 535–539. doi:10.1126/science.1222453.
- [6] J.-W. Kim, G. Sauti, R.J. Cano, R.A. Wincheski, J.G. Ratcliffe, M. Czabaj, N.W. Gardner, E.J. Siochi, Assessment of carbon nanotube yarns as reinforcement for composite overwrapped pressure vessels, *Compos. Part A*. 84 (2016) 256–265. doi:10.1016/j.compositesa.2016.02.003.
  - [7] Z. Li, J.G. Park, Z. Liang, High-Performance Multifunctional Thermoplastic Composites Enhanced by Aligned Buckypaper, *Adv. Eng. Mater.* 18 (2016) 1460–1468. doi:10.1002/adem.201600130.
  - [8] Q. Cheng, B. Wang, C. Zhang, Z. Liang, Functionalized carbon-nanotube sheet/bismaleimide nanocomposites: Mechanical and electrical performance beyond carbon-fiber composites, *Small*. 6 (2010) 763–767. doi:10.1002/smll.200901957.
  - [9] R.D. Downes, A. Hao, J.G. Park, Y.-F. Su, R. Liang, B.D. Jensen, E.J. Siochi, K.E. Wise, Geometrically constrained self-assembly and crystal packing of flattened and aligned carbon nanotubes, *Carbon*. 93 (2015) 953–966. doi:10.1016/j.carbon.2015.06.012.
  - [10] A. Thess, R. Lee, P. Nikolaev, H. Dai, Crystalline ropes of metallic carbon nanotubes, *Science*. 273 (1996) 483.
  - [11] S. Trayner, A. Hao, R. Downes, J.G. Park, Y.F. Su, R. Liang, High-resolution TEM analysis of flattened carbon nanotube packing in nanocomposites, *Synth. Met.* 204 (2015) 103–109. doi:10.1016/j.synthmet.2015.03.005.
  - [12] S. Li, J.G. Park, Z. Liang, T. Siegrist, T. Liu, M. Zhang, Q. Cheng, B. Wang, C. Zhang, In situ characterization of structural changes and the fraction of aligned carbon nanotube networks produced by stretching, *Carbon*. 50 (2012) 3859–3867. doi:10.1016/j.carbon.2012.04.029.
  - [13] B.D. Jensen, K.E. Wise, G.M. Odegard, Simulation of mechanical performance limits and failure of carbon nanotube composites, *Model. Simul. Mater. Sci. Eng.* 24 (2016) 25012. doi:10.1088/0965-0393/24/2/025012.
  - [14] Y. Lin, J.-W. Kim, J.W. Connell, M. Lebrón-Colón, E.J. Siochi, Purification of Carbon Nanotube Sheets, *Adv. Eng. Mater.* 17 (2015) 674–688. doi:10.1002/adem.201400306.
  - [15] M.G. Fyta, P.C. Kelires, Simulations of composite carbon films with nanotube inclusions, *Appl. Phys. Lett.* 86 (2005) 1–3. doi:10.1063/1.1924881.
  - [16] M. Fyta, P.C. Kelires, Simulations on the elastic response of amorphous and nanocomposite carbon, *Diam. Relat. Mater.* 16 (2007) 1676–1681. doi:10.1016/j.diamond.2007.03.001.
  - [17] C.F. Cornwell, C.R. Welch, Very-high-strength (60-GPa) carbon nanotube fiber design based on molecular dynamics simulations, *J. Chem. Phys.* 134 (2011). doi:10.1063/1.3594197.
  - [18] D.M. Mulvihill, N.P. O'Brien, W.A. Curtin, M.A. McCarthy, Potential routes to stronger carbon nanotube fibres via carbon ion irradiation and deposition, *Carbon*. 96 (2016) 1138–1156. doi:10.1016/j.carbon.2015.10.055.
  - [19] A. Kis, G. Csányi, J.-P. Salvetat, T.-N. Lee, E. Couteau, A.J. Kulik, W. Benoit, J. Brugger, L. Forró, Reinforcement of single-walled carbon nanotube bundles by intertube bridging, *Nat. Mater.* 3 (2004) 153–157. doi:10.1038/nmat1076.



- [20] M. Locascio, B. Peng, P. Zapol, Y. Zhu, S. Li, T. Belytschko, H.D. Espinosa, Tailoring the load carrying capacity of MWCNTs through Inter-shell atomic bridging, *Exp. Mech.* 49 (2009) 169–182. doi:10.1007/s11340-008-9216-3.
- [21] N.P. O'Brien, M.A. McCarthy, W.A. Curtin, A theoretical quantification of the possible improvement in the mechanical properties of carbon nanotube bundles by carbon ion irradiation, *Carbon*. 53 (2013) 346–356. doi:10.1016/j.carbon.2012.11.021.
- [22] S.K. Pregler, S.B. Sinnott, Molecular dynamics simulations of electron and ion beam irradiation of multiwalled carbon nanotubes: The effects on failure by inner tube sliding, *Phys. Rev. B*. 73 (2006) 224106. <http://link.aps.org/doi/10.1103/PhysRevB.73.224106>.
- [23] R.L. Federizzi, C.S. Moura, L. Amaral, Polymerization of Carbon Nanotubes through Self-Irradiation, *J. Phys. Chem. B*. 110 (2006) 23215–23220. doi:10.1021/jp064907g.
- [24] A.C.T. van Duin, S. Dasgupta, F. Lorant, W.A. Goddard III, ReaxFF: A reactive force field for hydrocarbons, *J. Phys. Chem. A*. 105 (2001) 9396–9409. doi:10.1021/jp004368u.
- [25] S. Goverapet Srinivasan, A.C.T. van Duin, P. Ganesh, Development of a ReaxFF potential for carbon condensed phases and its application to the thermal fragmentation of a large fullerene, *J. Phys. Chem. A*. 119 (2015) 571–580. doi:10.1021/jp510274e.
- [26] B.D. Jensen, K.E. Wise, G.M. Odegard, Simulation of the Elastic and Ultimate Tensile Properties of Diamond, Graphene, Carbon Nanotubes, and Amorphous Carbon Using a Revised ReaxFF Parametrization, *J. Phys. Chem. A*. 119 (2015) 9710–9721. doi:10.1021/acs.jpca.5b05889.
- [27] B.D. Jensen, K.E. Wise, G.M. Odegard, The effect of time step, thermostat, and strain rate on ReaxFF simulations of mechanical failure in diamond, graphene, and carbon nanotube., *J. Comput. Chem.* 36 (2015) 1587–1596. doi:10.1002/jcc.23970.
- [28] T.P. Senftle, S. Hong, M.M. Islam, S.B. Kylasa, Y. Zheng, Y.K. Shin, C. Junkermeier, R. Engel-Herbert, M.J. Janik, H.M. Aktulga, T. Verstraelen, A. Grama, A.C.T. van Duin, T. P. Senftle, S. Hong, M.M. Islam, S.B. Kylasa, Y. Zheng, Y.K. Shin, C. Junkermeier, R. Engel-Herbert, M.J. Janik, H.M. Aktulga, T. Verstraelen, A. Grama, A.C.T. van Duin, The ReaxFF reactive force-field: development, applications and future directions, *Npj Comput. Mater.* 2 (2016) 15011. doi:10.1038/npjcompumats.2015.11.
- [29] S. Plimpton, Fast Parallel Algorithms for Short – Range Molecular Dynamics, *J. Comput. Phys.* 117 (1995) 1–42. doi:10.1006/jcph.1995.1039.
- [30] H.M. Aktulga, J.C. Fogarty, S.A. Pandit, A.Y. Grama, Parallel reactive molecular dynamics: Numerical methods and algorithmic techniques, *Parallel Comput.* 38 (2012) 245–259. doi:10.1016/j.parco.2011.08.005.
- [31] K. Yoon, A. Ostadhossain, A.C.T. van Duin, Atomistic-scale simulations of the chemomechanical behavior of graphene under nanoparticle impact, *Carbon*. 99 (2016) 58–64. doi:10.1016/j.carbon.2015.11.052.
- [32] J.M.H. Kroes, F. Pietrucci, A.C.T. van Duin, W. Andreoni, Atom Vacancies on a Carbon Nanotube: To What Extent Can We Simulate their Effects?, *J. Chem. Theory*

- Comput. 11 (2015) 3393–3400. doi:10.1021/acs.jctc.5b00292.
- [33] M.M. Islam, C. Zou, A.C.T. van Duin, S. Raman, Interactions of hydrogen with the iron and iron carbide interfaces: a ReaxFF molecular dynamics study, *Phys. Chem. Chem. Phys.* 18 (2016) 761–771. doi:10.1039/C5CP06108C.
  - [34] S.J. Pai, B.C. Yeo, S.S. Han, Development of the ReaxFFCBN reactive force field for the improved design of liquid CBN hydrogen storage materials, *Phys. Chem. Chem. Phys.* 18 (2016) 1818–1827. doi:10.1039/C5CP05486A.
  - [35] F. Tavazza, T.P. Senftle, C. Zou, C.A. Becker, A.C.T. van Duin, Molecular Dynamics Investigation of the Effects of Tip-Substrate Interactions during Nanoindentation, *J. Phys. Chem. C* 119 (2015) 13580–13589. doi:10.1021/acs.jpcc.5b01275.
  - [36] C. Ashraf, A.C.T. van Duin, Extension of the ReaxFF Combustion Force Field toward Syngas Combustion and Initial Oxidation Kinetics, *J. Phys. Chem. A* 121 (2017) 1051–1068. doi:10.1021/acs.jpca.6b12429.
  - [37] A. Stukowski, Visualization and analysis of atomistic simulation data with OVITO—the Open Visualization Tool, *Model. Simul. Mater. Sci. Eng.* 18 (2009) 15012. doi:10.1088/0965-0393/18/1/015012.
  - [38] R.F. Gibson, *Principles of composite material mechanics*, CRC press, 2016.
  - [39] Z. Cui, S. Yang, L.C. Brinson, Fast evaluation of local elastic constants and its application to nanosized structures, *Phys. Rev. B* 91 (2015). doi:10.1103/PhysRevB.91.184104.
  - [40] H. Mizuno, S. Mossa, J.-L. Barrat, Measuring spatial distribution of the local elastic modulus in glasses, *Phys. Rev. E* 87 (2013) 42306. doi:10.1103/PhysRevE.87.042306.
  - [41] J.-W. Kim, G. Sauti, E.J. Siochi, J.G. Smith, R.A. Wincheski, R.J. Cano, J.W. Connell, K.E. Wise, Toward high performance thermoset/carbon nanotube sheet nanocomposites via resistive heating assisted infiltration and cure, *ACS Appl. Mater. Interfaces* 6 (2014) 18832–18843. doi:10.1021/am5046718.
  - [42] E.J. Siochi, R.J. Cano, R.A. Wincheski, J.G. Ratcliffe, B.D. Jensen, K.E. Wise, J. Kim, G. Sauti, High Volume Fraction Carbon Nanotube Composites for Aerospace Applications, in: *CAMX 2015 - Compos. Adv. Mater. Expo*, Dallas, TX, 2015: pp. 1122–1132.
  - [43] K. Koziol, J. Vilatela, A. Moisala, M. Motta, P. Cuniff, M. Sennett, A. Windle, High-performance carbon nanotube fiber., *Science* 318 (2007) 1892–1895. doi:10.1126/science.1147635.
  - [44] I. Ostanin, R. Ballarini, D. Potyondy, T. Dumitrică, A distinct element method for large scale simulations of carbon nanotube assemblies, *J. Mech. Phys. Solids* 61 (2013) 762–782. doi:10.1016/j.jmps.2012.10.016.
  - [45] A.N. Volkov, L. V. Zhigilei, Mesoscopic interaction potential for carbon nanotubes of arbitrary length and orientation, *J. Phys. Chem. C* 114 (2010) 5513–5531. doi:10.1021/jp906142h.

# Supplemental information

## Simulating the effects of carbon nanotube continuity and interfacial bonding on composite strength and stiffness

Benjamin D. Jensen<sup>a\*</sup>, Gregory M. Odegard<sup>b</sup>, Jae-Woo Kim<sup>c</sup>, Godfrey Sauti<sup>a</sup>, Emilie J. Siochi<sup>a</sup>, Kristopher E. Wise<sup>a</sup>

<sup>a</sup> Advanced Materials and Processing Branch, NASA Langley Research Center, Hampton, VA USA

<sup>b</sup> Department of Mechanical Engineering - Engineering Mechanics, Michigan Technological University, Houghton, MI USA

<sup>c</sup> National Institute of Aerospace, Hampton, VA USA

\*Corresponding author: Benjamin Jensen, benjamin.d.jensen@nasa.gov

### Additional experimental details

The unprocessed carbon nanotube (CNT) yarn (Nanocomp Technologies, Inc.) used to fabricate the composite has a specific modulus of 31.847 GPa/(g/cm<sup>3</sup>), specific strength of 1.322 GPa/(g/cm<sup>3</sup>), and a linear density of 8.5 g/km. The CNT yarn composite was processed by resistive heating assisted infiltration with 20 mg/ml BMI (RM-3010, Renegade Materials Corp.) in toluene and then subjected to a thermal cure at 240 °C for 6 hrs. Three specimens were fabricated and mechanically tested, each with a gage length of 10 mm. Mechanical tests were performed with a crosshead speed of 0.5 mm/min. After composite fabrication, the CNT/BMI composite yarn had a linear density of 10.4 g/km.

### Additional computational details

Because the simulated systems contain only carbon atoms, no significant atomic charges were found to arise in test simulations. Based on this observation, all atomic charges were set to zero and the charge equilibration scheme was disabled in all production runs, resulting in a substantial increase in simulation speed. To maintain consistency with the authors' previously published results for related systems, a prepublication version of the ReaxFF<sub>C-2013</sub> parameter set was used in this work. Small changes made to some parameters prior to final publication had an insignificant impact on the properties of interest in this work.[1,2]

All systems were composed of two bundles of seven tubes, and an amorphous carbon (AC) matrix with an AC:CNT mass ratio of 167:100 and CNT volume fractions near 50%. After equilibration, the average density of the matrix (including the interface) for each system was found to be approximately 2.4 g/cm<sup>3</sup> for the continuous systems and approximately 2.2

$\text{g}/\text{cm}^3$  in the discontinuous systems, due to the additional volume from the 2 nm spacing between CNT end-caps. The continuous systems contained 71,890 atoms and the discontinuous systems contained 154,604 atoms. For the continuous systems, the size of the simulation box and the spacing between CNT bundles were set to meet two requirements: the specified AC:CNT mass ratio and an initial AC density of  $3.0 \text{ g}/\text{cm}^3$ . The two independent discontinuous systems were created with different CNT translations, resulting in different spacing of neighboring CNT ends

The equilibration procedure began with 32 ps of energy minimization at low temperature, followed by heating the system to 1,200 K in 60 ps and equilibrating it at 1,200 K for 150 ps, and then cooling the system back to 300 K in 90 ps. This was followed by two additional 110 ps heating and cooling cycles.

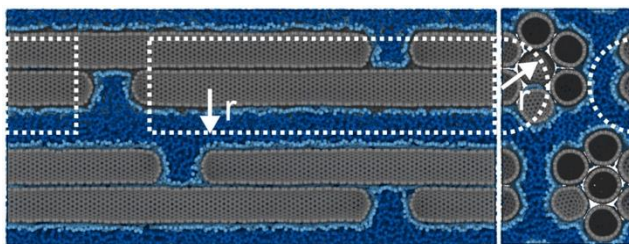


Fig. S1. Representative cylinder used for computing cylindrical distribution function in discontinuous CNT composites.

The cylindrical distribution function is analogous to the more commonly encountered radial distribution function, but concentric cylindrical, rather than radial, shells are used to quantify the matrix atom number density adjacent to the outermost CNTs in the bundles. The zero radius point in Fig. 4c and 4d is placed at the CNT wall. As shown in Fig. S1, the cylindrical distribution functions for the discontinuous systems are computed only along the middle length of each CNT, terminating before the endcaps to avoid ambiguity in the end cap region. So while the endcaps and matrix gap between the ends are excluded from the distribution function of a particular CNT, those of neighboring CNT endcaps and AC gaps are still included in the computation, making the discontinuous CNT cylindrical distribution function comparable to that of the continuous systems.

### Additional crosslink details

The crosslinking fraction is determined by summing the number of CNT atoms covalently bonded to a matrix atom and dividing by the number of CNT atoms directly exposed to the matrix, defined as the matrix-facing  $2/3$  of the outer six nanotubes in each bundle. In the case of discontinuous CNTs,  $2/3$  of the end-cap atoms are also included in the number density calculation. Initial crosslink sites are selected at random from a list of candidate CNT atoms, and the crosslinks created by placing an AC atom within bonding distance of the selected CNT atom at the beginning of the equilibration procedure. Because ReaxFF is used, pre-seeded crosslinks are free to break and new crosslinks may form during the equilibration process, resulting in degrees of crosslinking that differ somewhat from the nominal value during the simulations. For the same reason, the nominally 0% crosslinked

systems are found to have a very small amount of crosslinking, typically in the range of 0.1%-0.4%, which are referred to as <1% crosslink systems.

Examples of crosslinks are shown in Fig. S2a and Fig. S2b for the 4% and 19% crosslinked discontinuous systems. Crosslinks between the CNTs and AC matrix are typically 3 coordinate, with one covalent bond to a CNT atom and two covalent bonds to matrix atoms. Crosslinks in which the matrix atom has 2 coordinate bonding are occasionally found in situations with sterically restricted geometries, such as the crevice between two CNTs. The majority of the CNT atoms involved in crosslinks are found in a 4 coordinate configuration. In some cases, typically the high crosslink density systems, clusters of neighboring crosslink sites can create an opening in the CNT sidewall. In these cases, the crosslinked CNT atoms remain in a 3 coordinate bonding configuration.

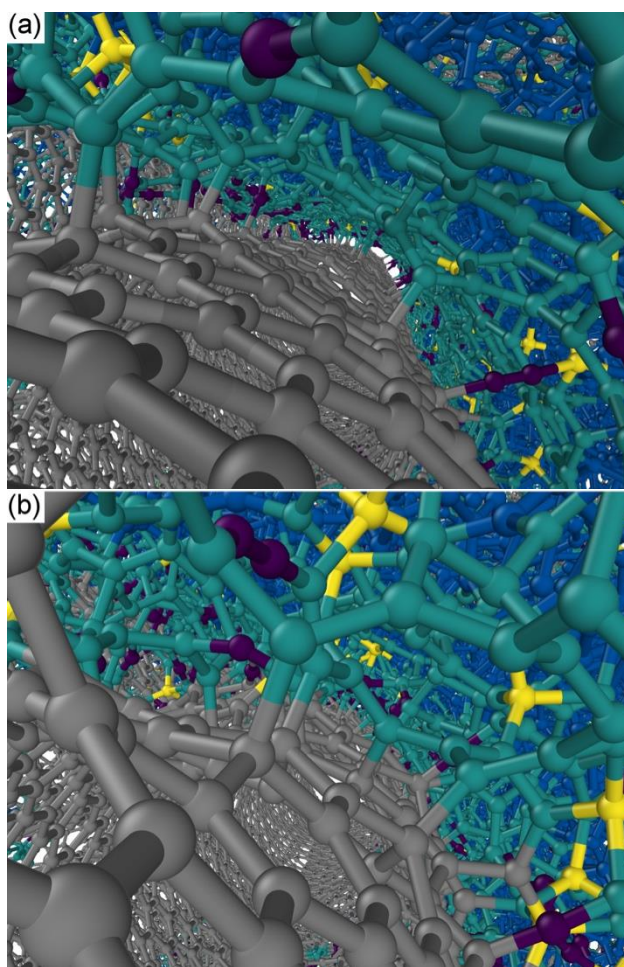


Fig. S2. CNT-AC crosslinks in the (a) 4% and (b) 19% crosslinked discontinuous systems.

Atoms in the interface layer are colored according to their atomic bonding with 4 coordinate shown in light yellow, 3 coordinate in teal, and 2 coordinate in dark purple.

CNT and bulk matrix atoms are colored as in Fig. 1



## Calculation of the CNT Constituent Strain and Modulus in Discontinuous Systems

The calculation of the axial specific modulus of the discontinuous nanotube and corresponding matrix interface constituents, shown in Fig. 3b and Fig. 3c of the main paper, assumes a non-continuous particle/matrix interface in which the void space that appears at the tube ends under deformation is attributed to neither constituent. If, instead, one wanted to treat the CNT-void-matrix region in a continuous manner, the void space would have to be attributed to either the CNT or matrix. Some authors have chosen to combine the void space with the matrix interface, referred to as an *effective interface* [3–7], while others have chosen to combine it with the nanoparticle, which is referred to as an *effective nanoparticle* [8,9]. This second approach essentially treats the CNTs as if they had been strained by an amount equivalent to the global strain.

Fig. S3 compares the results of computing the CNT constituent modulus using the *effective nanoparticle* approach (purple line) to the discrete CNT method used in the paper (gray line). At the highest degree of crosslinking, for which essentially no gap opens at the CNT tube end-matrix interface, the calculated moduli are very similar, as expected. As the degree of crosslinking decrease and the size of the void increases, the moduli calculated using the two methods begin to differ.

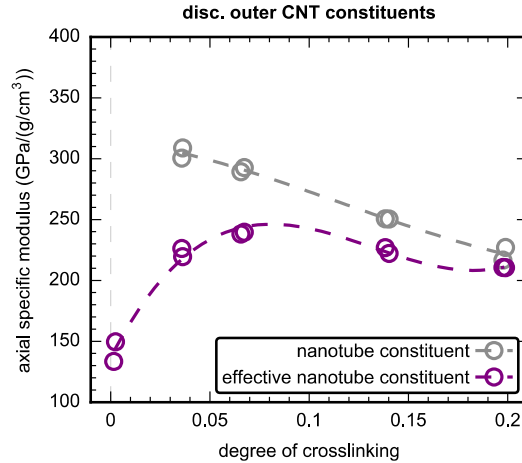


Fig. S3. Effective discontinuous outer CNT specific modulus. The discontinuous CNT moduli from Fig. 3b in the main text is replotted here (gray line) for comparison purposes.

## Transverse and shear elastic properties

The transverse stiffness of the continuous and discontinuous systems is compared for different crosslink fractions in Fig. S4. The near overlap of these two plots demonstrates that the transverse specific stiffness is not substantially affected by the continuity of the CNTs. In both systems the stiffness increases by approximately 50%, from around 24 GPa/(g/cm³) at <1% crosslinking to a maximum of 36 GPa/(g/cm³) at ~15% crosslinking, after which there is no benefit from additional crosslinking. It is also interesting to note that, even at the maximum extent of crosslinking considered in this work, the transverse

specific stiffness is only ~35% of that found for the bulk matrix in the axial simulations, meaning the CNT bundles essentially act as defects in the transverse direction. This is a result of the high stiffness of amorphous carbon and because the bundles easily pull apart, since no direct crosslinks are formed between the CNTs that comprise the bundles.

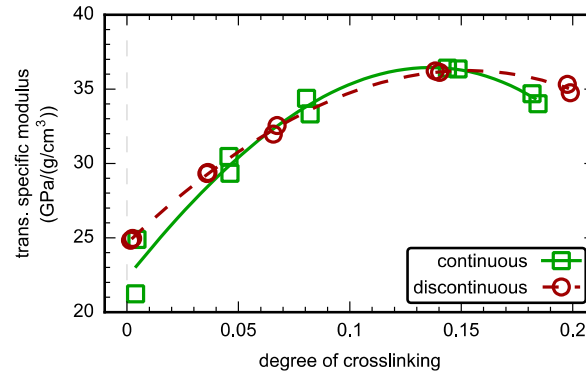


Fig. S4. Transverse specific modulus as a function of degree of crosslinking. Trendlines are a guide to the eye.

The in-plane shear modulus, corresponding to shear deformations along the CNT axes, is the most frequently reported component of the shear modulus for planar composites. As shown in Fig. S5a, the continuous and discontinuous systems exhibit very similar trends for in-plane shear modulus with increasing crosslinking. Both composites increase in stiffness by ~48% across the range of crosslinking considered, although the modulus of the continuous system is consistently ~5 GPa/(g/cm³) higher. The constituent shear moduli are computed using Eq. 1, with global strains, due to the challenge of determining local strains at the CNT-matrix interface. Examination of the constituent moduli reveal that this is largely the result of differences in the structured interfacial layer and CNT properties. At low degrees of crosslinking, the more highly structured interface in the continuous composite, is primarily responsible for the higher composite property. As crosslinking is increased, the effects of the higher interfacial structuring diminish and the higher modulus of the continuous CNTs is apparent. The specific out-of-plane shear modulus and major Poisson's ratio, and minor Poisson's ratio are not strongly dependent on the continuity of the CNTs, reflected in their similar crosslinking responses shown in Fig. S6, SI7 and SI8 respectively.

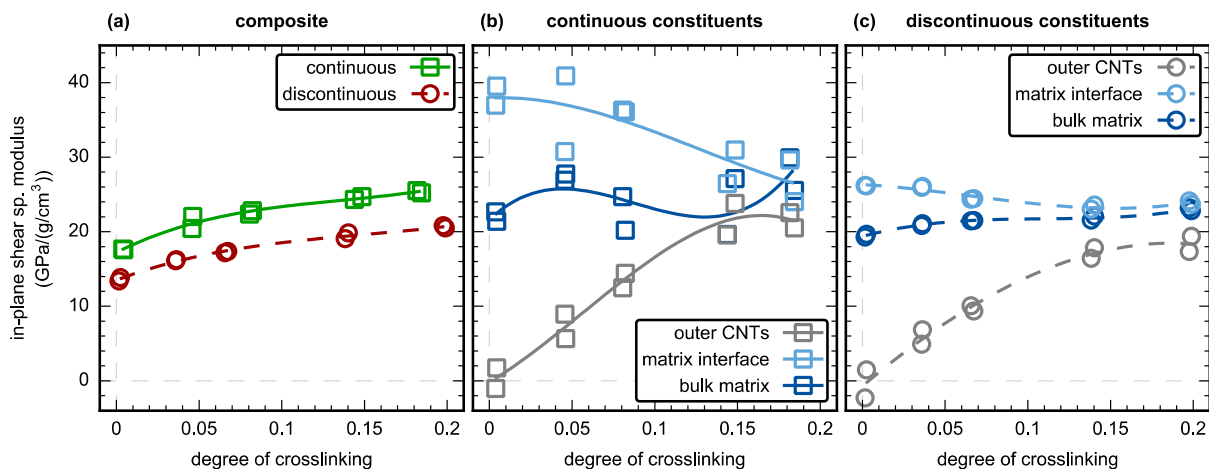


Fig. S5. In-plane specific shear modulus of the (a) composites, (b) continuous CNT constituents and (c) discontinuous CNT constituents as a function of degree of crosslinking. Trendlines are a guide to the eye. Center CNT moduli were near zero for both systems and are excluded for clarity.

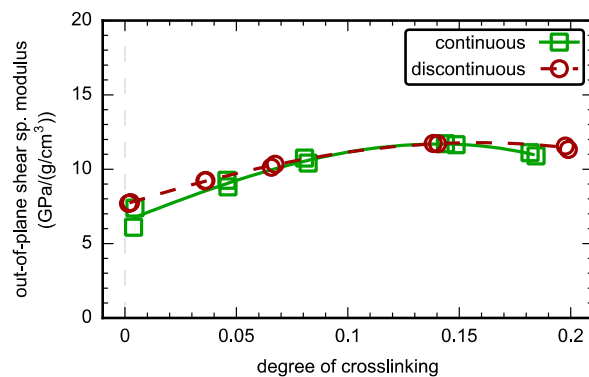


Fig. S6. Out-of-plane specific shear modulus of the (a) composites, (b) continuous CNT constituents and (c) discontinuous CNT constituents as a function of degree of crosslinking. Trendlines are a guide to the eye. Outer and inner CNT properties are similar and are combined to create “all CNTs” data points.



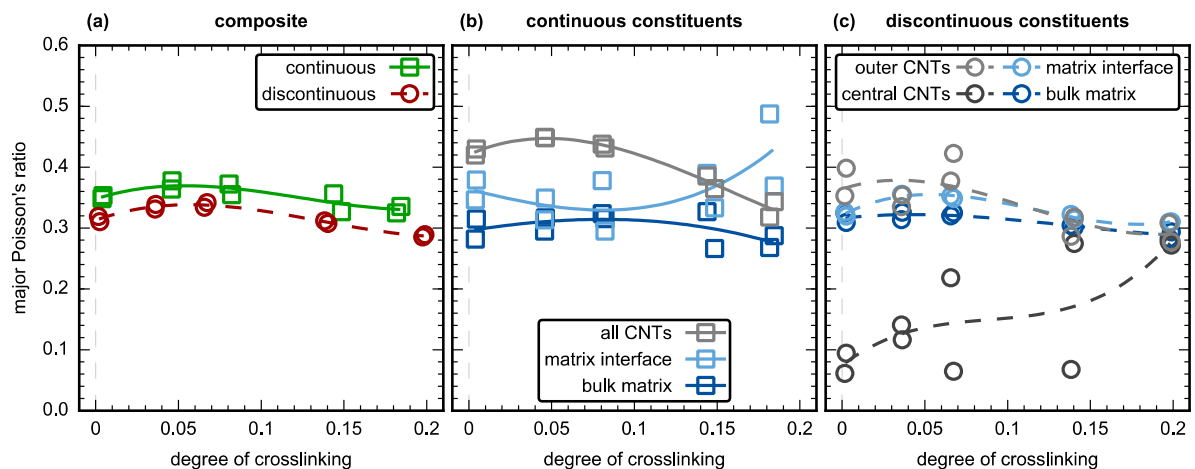


Fig. S7. Major Poisson's ratio of the (a) composites, (b) continuous CNT constituents and (c) discontinuous CNT constituents as a function of degree of crosslinking. Outer and inner continuous CNT properties are similar and are combined to create "all CNTs" data points.

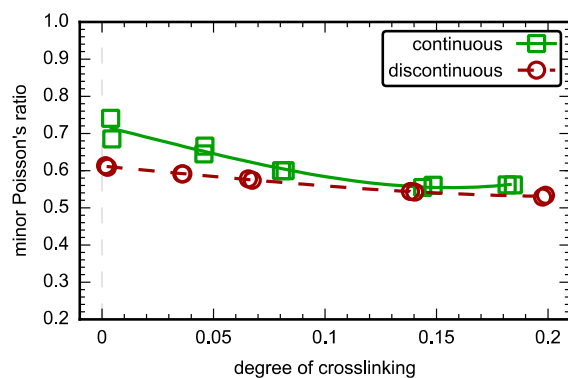


Fig. S8. Minor Poisson's ratio of the (a) composites, (b) continuous CNT constituents and (c) discontinuous CNT constituents as a function of degree of crosslinking. Outer and inner CNT properties are similar and are combined to create "all CNTs" data points.

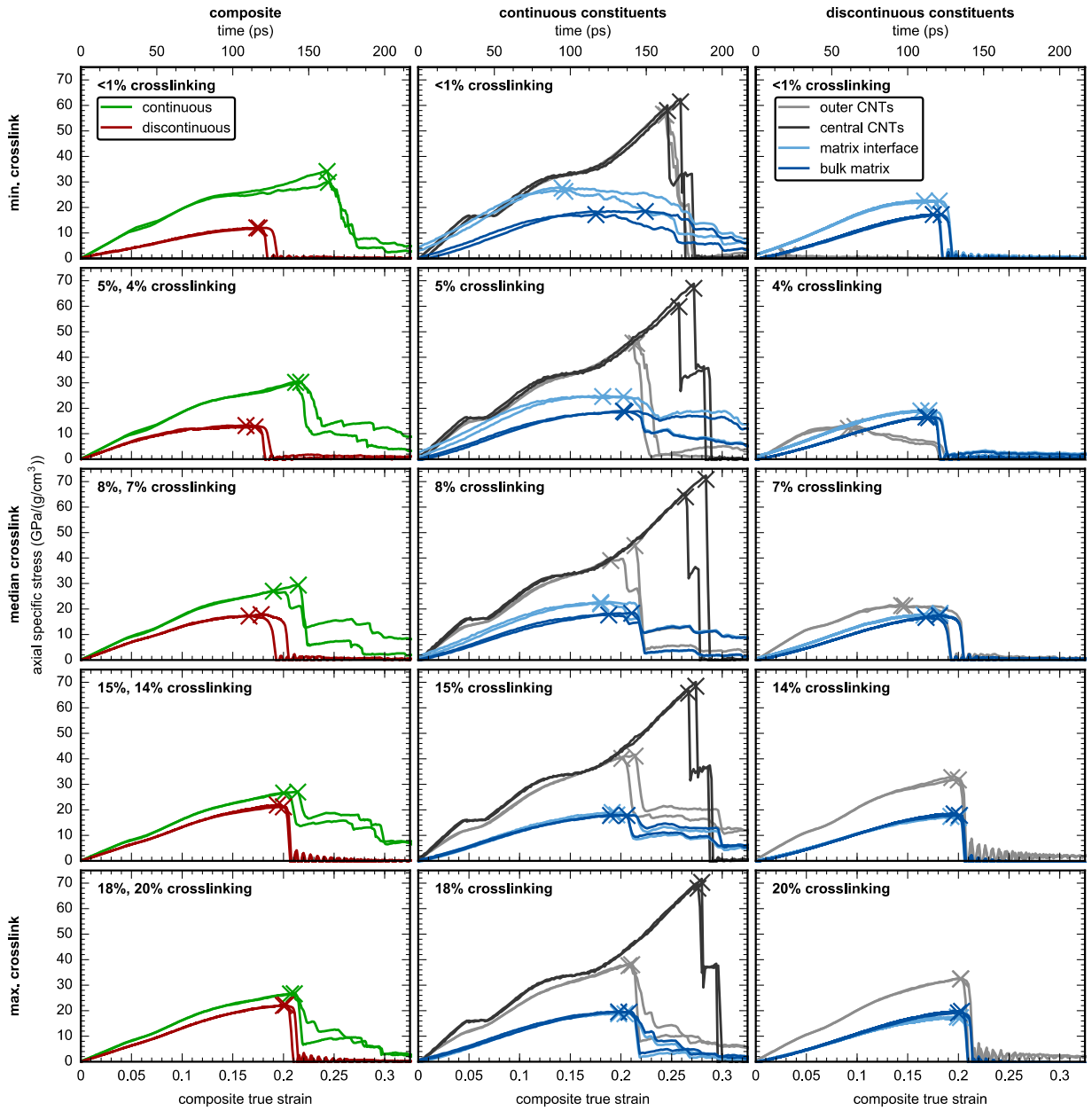


Fig. S9. Axial specific stress strain response of all composite systems and their constituents

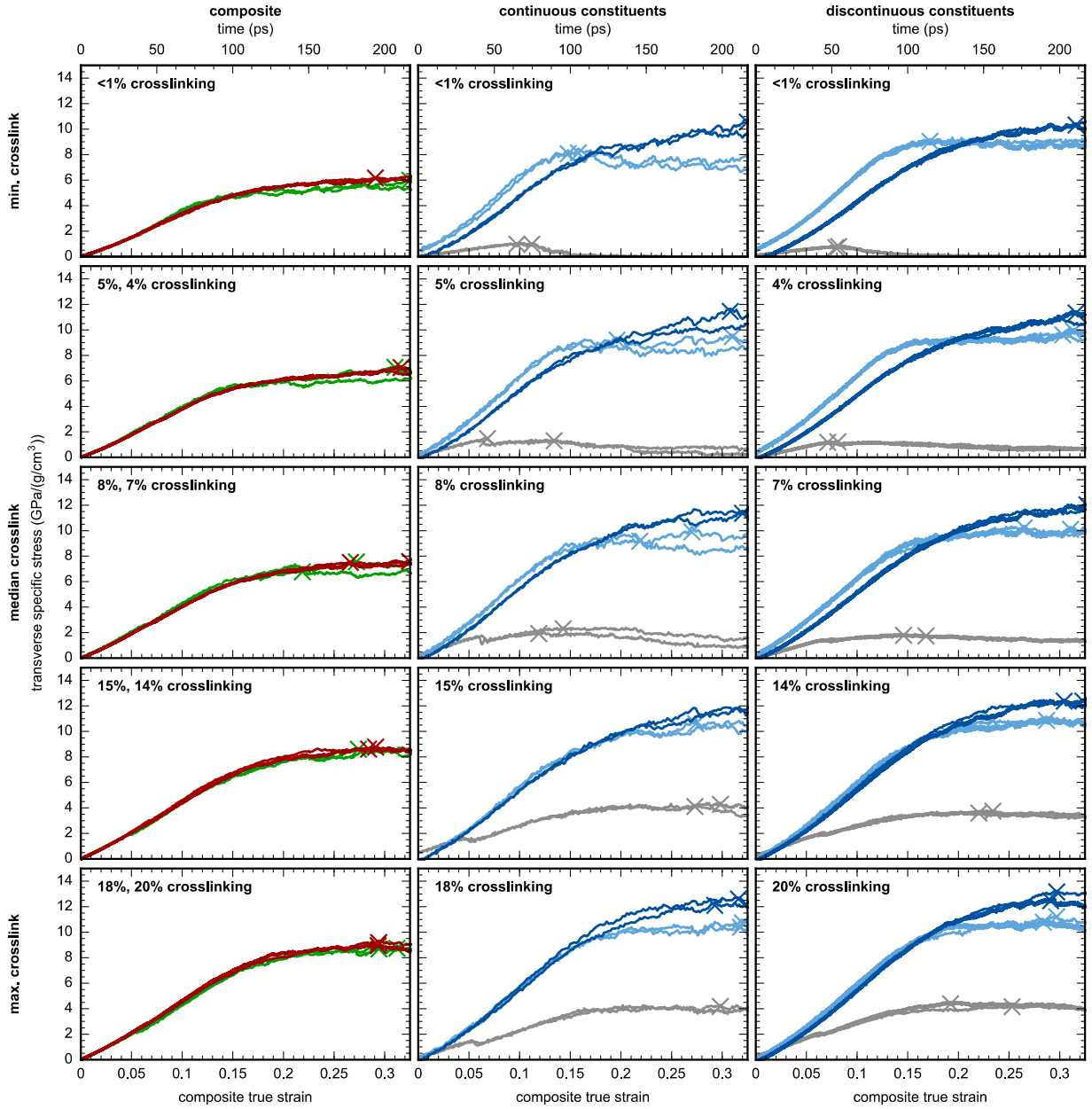


Fig. S10. Transverse specific stress strain response of all composite systems and their constituents.

The transverse specific ultimate stresses for continuous and discontinuous systems are compared for varying degrees of crosslinking in Fig. S11. The specific ultimate stresses increase by approximately 50%, from 6 GPa/(g/cm<sup>3</sup>) to 9 GPa/(g/cm<sup>3</sup>), from the lowest to highest crosslinking fractions. This comparable response indicates that CNT continuity does not substantially influence the transverse specific ultimate stresses.

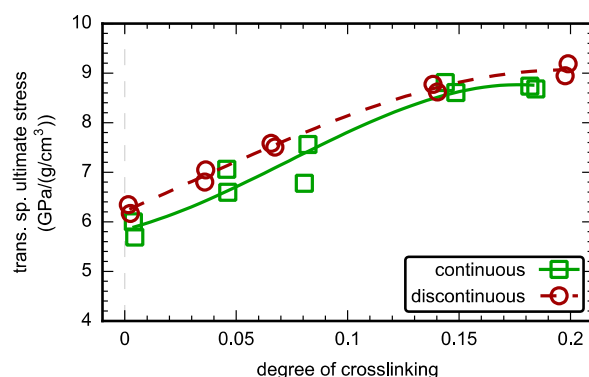


Fig. S11. Transverse specific ultimate stress as a function of degree of crosslinking. Trendlines are a guide to the eye.

## References

- [1] B.D. Jensen, K.E. Wise, G.M. Odegard, Simulation of mechanical performance limits and failure of carbon nanotube composites, *Model. Simul. Mater. Sci. Eng.* 24 (2016) 25012. doi:10.1088/0965-0393/24/2/025012.
- [2] B.D. Jensen, K.E. Wise, G.M. Odegard, Simulation of the Elastic and Ultimate Tensile Properties of Diamond, Graphene, Carbon Nanotubes, and Amorphous Carbon Using a Revised ReaxFF Parametrization, *J. Phys. Chem. A.* 199 (2015) 9710–9721. doi:10.1021/acs.jpca.5b05889.
- [3] M.M. Shokrieh, R. Rafiee, On the tensile behavior of an embedded carbon nanotube in polymer matrix with non-bonded interphase region, *Compos. Struct.* 92 (2010) 647–652. doi:10.1016/j.compstruct.2009.09.033.
- [4] G.M. Odegard, T.C. Clancy, T.S. Gates, Modeling of the mechanical properties of nanoparticle/polymer composites, *Polymer.* 46 (2005) 553–562. doi:10.1016/j.polymer.2004.11.022.
- [5] J. Choi, H. Shin, M. Cho, A multiscale mechanical model for the effective interphase of SWNT/epoxy nanocomposite, *Polymer.* 89 (2016) 159–171. doi:10.1016/j.polymer.2016.02.041.
- [6] B. Kim, J. Choi, S. Yang, S. Yu, M. Cho, Multiscale modeling of interphase in crosslinked epoxy nanocomposites, *Compos. Part B.* 120 (2017) 128–142. doi:10.1016/j.compositesb.2017.03.059.
- [7] H.W. Wang, H.W. Zhou, R.D. Peng, L. Mishnaevsky, Nanoreinforced polymer composites: 3D FEM modeling with effective interface concept, *Compos. Sci. Technol.* 71 (2011) 980–988. doi:10.1016/j.compscitech.2011.03.003.
- [8] G.M. Odegard, T.S. Gates, K.E. Wise, C. Park, E.J. Siochi, Constitutive modeling of nanotube-reinforced polymer composites, *Compos. Sci. Technol.* 63 (2003) 1671–1687. doi:10.1016/S0266-3538(03)00063-0.

- [9] G.M. Odegard, S.-J. V Frankland, T.S. Gates, Effect of Nanotube Functionalization on the Elastic Properties of Polyethylene Nanotube Composites, *AIAA J.* 43 (2005) 1828–1835. doi:10.2514/1.9468.